Soft Matter

Volume 1 | Number 1 | Jan 2013 | Pages 1–100

Soft Matter

www.rsc.org/softmatter

ROYAL SOCIETY
OF CHEMISTRY

www.rsc.org/softmatter

ARTICLE TYPE

Smoothing of Contact Lines in Spreading Droplets by Trisiloxane Surfactants and its Relevance for Superspreading[†]

Rolf E. Isele-Holder,[*a,b§] **Benjamin Berkels,**[b¶] **and Ahmed E. Ismail**[*a,b‡]

Superspreading, the greatly enhanced spreading of aqueous solutions of trisiloxane surfactants on hydrophobic substrates, is of great interest in fundamental physics and technical applications. Despite numerous studies in the last 20 years, the superspreading mechanism is still not well understood, largely because the molecular scale cannot be resolved appropriately either experimentally or using continuum simulations. The absence of molecular-scale knowledge has led to a series of conflicting hypotheses based on different assumptions of surfactant behavior. We report a series of large-scale molecular dynamics simulations of aqueous solutions of superspreading and non-superspreading surfactants on different substrates. We find that the transition from the liquid–vapor to the solid–liquid interface is smooth for superspreading conditions, allowing direct adsorption through the contact line. This finding complements a study [Karapetsas et al., *J. Fluid Mech.*, **2011**, *670*, 5–37], which predicts that superspreading can occur if this adsorption path is possible. Based on the observed mechanism, we provide plausible explanations for the influence of the substrate hydrophobicity, the surfactant chain length, and the surfactant concentration on the superspreading phenomenon. We also briefly address that the observed droplet shape is a mechanism to overcome the Huh–Scriven paradox of infinite viscous dissipation at the contact line.

1 Introduction

Superspreading is the ultra-rapid wetting of aqueous droplets on hydrophobic substrates enabled by trisiloxane surfactants. Dependent on the substrate hydrophobicity, the chain length of the hydrophilic tail, and the surfactant concentration, superspreading is maximized for intermediate values of all of these factors, and vanishes if any factor deviates too far from its optimum. Notably, the surfactant concentration for maximal spreading rates occurs just below a bulk-phase transition from surfactant vesicles to lamellar phases.[1–8] Superspreading is the only known mechanism, with the possible exception of voltage-induced spreading,[9] that can lead to rapid spreading.[10] It is therefore highly relevant to both fundamental physics, because of the violation of typically known spreading laws, and to industrial applications, because of the need to optimize the effect and to develop alternative superspreading agents, as current superspreading agents are known to be

toxic.[11] While the phenomenon has been extensively studied in the last 20 years by numerous groups from both industry and academia, it is still not understood how or why trisiloxane surfactants facilitate superspreading.[3–5]

Spreading dynamics of droplets can often be described by a power law,

$$r \propto t^{\alpha}, \tag{1}$$

where r is the base radius of the droplet, t is the time, and α is the spreading exponent characterizing the spreading regime, which results from a balance of driving and refraining forces and depends on the underlying physics.[10] For small droplets, the driving force is typically differences in surface free energies, whereas the refraining force can vary. After depositing a droplet on a substrate, the spreading passes through different regimes. Right after deposition, the refraining force is inertia; the spreading exponent in this regime is $1/5 \leq \alpha \leq 1/2$.[12] After a characteristic time that depends on the droplet size and fluid properties, the spreading decelerates and the droplet enters a second regime, in which the refraining force is viscous dissipation at the contact line. Lubrication theory and the no-slip boundary condition between the substrate and the droplet predict the Huh–Scriven paradox of logarithmically diverging viscous dissipation at the contact line.[10,13] Obviously, these approximations must break down at the contact line because such a result conflicts with the observed spreading of droplets. However, this finding illustrates why the region near the contact line is important for the viscous spreading regime.

Various models have been proposed to overcome the singularity at the contact line, the most commonly used of which are the hydrodynamic model (HDM) and molecular kinetic theory (MKT). In the HDM, singularities at the contact line are avoided by allowing slip.[10,14] In MKT, contact-line motion is described via molecular jumps.[15] The models predict different spreading exponents: HDM and MKT predict $\alpha_{3D,HDM} = 1/10$ and $\alpha_{3D,MKT} = 1/7$ in three dimensions, and $\alpha_{2D,HDM} = 1/7$ and $\alpha_{2D,MKT} = 1/5$ in two dimensions.[10,16] The 3D spreading exponent for the HDM corresponds to the most frequently observed spreading exponent and matches "Tanner's law".[10,17]

Recently, Wang et al.[18] showed that aqueous solutions of trisiloxane surfactants on hydrophobic substrates pass through the regimes described above. They observed two major differences between superspreading and non-superspreading solutions of trisiloxane surfactants. First, in the viscous spreading regime, the spreading exponent of non-superspreading surfactants agreed with Tanner's law, with $\alpha \approx 1/10$. For the superspreading surfactant, the spreading exponent was slightly larger, with a value of $\alpha \approx 1/7$. The authors concluded that the HDM describes non-superspreading wetting well, while the underlying mechanism for superspreading case in the viscous regime is closer to the MKT. Second, while spreading remained in the viscous regime for non-superspreading surfactants, superspreading droplets entered a third spreading regime, the superspreading regime. In their study, spreading exponents in this regime were $0.25 \lesssim \alpha \lesssim 0.5$. Other authors have measured similar or larger spreading exponents for this regime.[19]

While there is a debate about the relevant mechanisms of superspreading, there is a consensus that different effects pertain at both the micro- and macroscales. At the macroscopic scale, Marangoni stresses are the most frequently cited driving forces for superspreading, although other influences are also mentioned.[4,5,20] At the microscale, several molecular mechanisms have been proposed.[19,21–25] Apart from the theory of Kabalnov,[22] which attributes superspreading to large negative spreading coefficients facilitated by vesicle formation, the contact-line region of the droplet is commonly considered crucial for superspreading. Specifically, theories or models that explain superspreading are based on various assumptions: for instance, that vesicles unzip at the contact line[21], that a thick precursor stabilized by vesicles is formed,[23] that surfactants diffuse rapidly to the three-phase contact line from the bulk,[19] that surfactants adsorb directly from the liquid–vapor interface to the solid–liquid interface,[24] or that surfactants form a bilayer that precedes the droplet.[25]

For most proposed molecular mechanisms, it is unclear exactly how the hindrance of rapid spreading because of extreme viscous dissipation at the contact line should be resolved. However, Karapetsas et al.[24] showed in computational fluid dynamics simulations that the extreme dissipation can be overcome and superspreading can occur if Marangoni stresses arise and are maintained during spreading. In their study Marangoni stresses and surfactant concentrations gradients resulted from surfactants being both soluble and being able to adsorb directly through the contact line from the liquid surface to the solid–liquid interface. While the solubility of trisiloxane surfactants is well-known, it is unclear how direct adsorption through the contact line works; formation of a bilayer ahead of the droplet has been hypothesized.[24] The study proves that superspreading can be facilitated by Marangoni stresses but does not provide evidence for how these stresses develop and are maintained. The underlying molecular mechanisms remain subject to speculation.

As suggested by Maldarelli,[26] molecular dynamics (MD) simulations are required for further insights into the molecular mechanisms of superspreading. In 2001, McNamara et al.[27] reported spreading simulations of simple model molecules. They observed that surfactants can enhance wetting and that the contact-line region can exhibit a smooth transition instead of a sharp edge. The finding that surfactants can enhance wetting, especially when interactions between the substrate and the hydrophobic part of the surfactant are strong, is confirmed in simulations by Kim et al.[28] MD simulations directly connected to superspreading have already been performed by Shen et al.[29] and Halverson et al.[30] Shen et al. studied the effect of the surfactant shape using simple Lennard-Jones (LJ) model surfactants and found that T-shaped surfactants increase spreading velocities compared to linear ones. Moreover, the formation of bilayers was discovered, even though the model was relatively simple and the simulation contained only $\approx 10^4$ beads. The study by Halverson et al. used larger droplets and surfactant models that were supposed to be more realistic. However, their simulations disagreed with experiment because the model for the trisiloxane surfactant was inaccurate.[31]

Finally, in a recent MD study using a coarse-grained potential, formation of precursor bilayers was observed for the spreading of aqueous solutions of trisiloxane surfactants.[32] The coarse-grained model's capability of representing surfactant–water mixtures are demonstrated in the supporting information of Ref. 32. However, there it is also reported that the interaction energy of the trisiloxane head and the substrate was $\varepsilon_{M-CM} > 1.4\varepsilon/k_B$ and $\varepsilon_{D-CM} > 1.4\varepsilon/k_B$; the exact values were not reported. These values are much greater than the value of $\varepsilon_{M-CM} = 0.78\varepsilon/k_B$ and $\varepsilon_{D-CM} = 0.5953\varepsilon/k_B$ which would have been consistent with the rest of their model. The greatly increased attraction between the substrate and the hydrophobic part of the surfactant of course promotes contact between the trisiloxane head group and the substrate, which in their simulations manifests in the formation of bilayers. It is thus possible that their observation is an artefact caused by the modifications of the force field, and thus not reflective of the

actual behavior of superspreading droplets.

We report large-scale MD simulations of water droplets laden with different trisiloxane and alkyl ethoxylate surfactants on various substrates. Simulations were performed with molecular models that we developed for application to the superspreading problem.[33] We cover different conditions that correspond to superspreading and non-superspreading scenarios in experiment. Specifically, we cover substrates from too hydrophilic to too hydrophobic substrates and surfactants from too short to too long, an intermediate state in which superspreading occurs in experiment, and a reference simulation with alkyl ethoxylate surfactants. We emphasize that although the simulations are large-scale for an MD framework, the simulated droplets are still nanoscopic. Because superspreading involves macroscopic effects, namely Marangoni stresses, we cannot hope to capture the effect directly in our simulations. However, the molecular mechanisms underlying superspreading can be resolved on the nanoscale and are accessible from our simulations.

In Section 2, we describe the simulation setup and the methods used to analyze the simulations. In Section 3, we report a smooth contact-line transition for simulations at superspreading conditions similar to that observed by McNamara et al.[27] The relation of this mechanism to the Huh–Scriven paradox[13] is briefly addressed and the relevance to superspreading is discussed in Section 4. The observed mechanism complements the simulation study by Karapetsas et al.[24] and allows plausible explanations for the complex dependency of the superspreading mechanism on the surface energy of the substrate and the size of the surfactants. We offer our conclusions in Section 5.

2 Methods

2.1 Simulation Setup

We performed MD simulations with cylindrical droplets of aqueous solutions of different surfactants on different polymer substrates. Simulations were carried out in a three-dimensional domain with periodic boundary conditions in each dimension. The substrate was parallel to the xy-plane and the axis of the cylinder was in the y-direction. The cylindrical droplet shape was maintained using the periodic boundary condition in the y-direction. Simulations of cylindrical droplets are computationally less intensive than those of spherical droplets and avoid effects caused by line tension. Based on the work of Halverson et al.[30] where only minor differences were observed between cylindrical and spherical geometries in simulations of surfactant-enhanced wetting, we expect the usage of cylindrical instead of spherical droplets on simulation results to be of minor importance. A few properties, however, such as the spreading exponent, depend on

the droplet geometry and must be translated between simulation and experiments that are usually performed with spherical droplets.[16]

The interaction of all materials are described with our recently developed molecular model,[33] which combines the TIP4P/2005 water model[34] with quantum-chemistry based models for the surfactants and substrates.[35–38] This all-atom model uses fixed charges for Coulomb interactions and LJ and Buckingham potentials for van der Waals (vdW) interactions. Parameters for the water–surfactant and water–substrate vdW interactions were empirically optimized to reproduce structural, energetic, and dynamic properties of simple model molecules and then validated in simulations of surfactants at the water surface.[33]

Simulations were performed with three different polymer substrates: polypropylene (PP), poly(ethylene oxide) (PEO), and polytetrafluoroethylene (PTFE). These different substrates include a substrate that is too hydrophobic (PTFE), one that is just right (PP),[39] and another that is too hydrophilic (PEO) for superspreading. While spreading experiments with trisiloxane-laden water droplets on PEO are not available, the small contact angle of around $20°$ indicates that the material is too hydrophilic for superspreading.[3,40] To prepare the substrates, monodisperse polymer chains with $n_{mon,PP} = 101$, $n_{mon,PEO} = 50$, or $n_{mon,PTFE} = 101$ monomers were used to create amorphous bulk configurations with the polymer builder of the MAPS platform.[41] The size of the box was $50\text{Å} \times 80\text{Å} \times 30\text{Å}$. The number of chains were $n_{PP} = 30$, $n_{PEO} = 34$, and $n_{PTFE} = 31$. The bulk systems were equilibrated in the *NPT* ensemble at a pressure of 1 atm with variable box dimensions only in the z-direction. The simulation was run for 1 ns at 500 K, was then cooled down to 300 K within 1 ns and run for another nanosecond at 300 K. Afterwards, periodic boundary conditions were removed in the z-direction, the box length in z-direction was extended and the simulation was run for another 1.5 ns. The resulting slabs had a thickness of approximately 30 Å and were used to generate substrate materials for the spreading simulations. The resulting surfaces are atomistically smooth and have no patterns or significant mesoscale roughness that would impact the spreading behavior. We expect the effect of roughness on the atomistic scale to be of minor importance. The labels in the figures and tables below describing simulations on different substrates correspond to the polymer abbreviations introduced above.

We ran simulations with trisiloxane surfactants with $n = 3$, $n = 6$, and $n = 11$, and alkyl ethoxylate surfactants with $n = 6$ and $m = 11$ (see Figure 1). The simulations are labeled T3, T6, T11, and CE, respectively. This choice of surfactants covers trisiloxane surfactants that are too long, too short, and just right for superspreading[6] and one additional surfactant for comparison. Starting structures for the droplets were generated by creating a cylinder from equilibrated bulk configura-
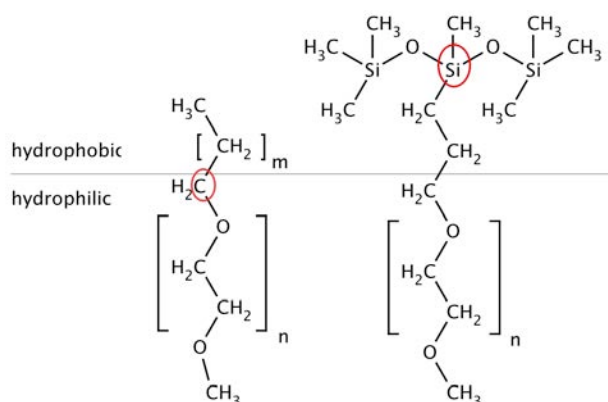
Fig. 1 Left: Alkyl ethoxylate and right: trisiloxane surfactants. The hydrophilic part of both surfactants is a poly(ethylene oxide) chain. The horizontal line separates the hydrophilic and the hydrophobic parts of each surfactant. Red circles label the central atoms used in the analysis.

tions of water. Surfactants were added to the surface to generate a fully covered droplet. Because trisiloxane surfactants are soluble, surfactants were added to the interior of the droplet to have a surfactant weight fraction $w_S \approx 0.02$ in the droplet interior in trisiloxane simulations, which is both well above the critical aggregate concentration of $w_S \approx 3 \times 10^{-5}$ and the critical wetting concentration of $w_s \approx 3 \times 10^{-3}$ for the onset of superspreading as defined and measured for T6 surfactants with an OH end group in Refs. 42 and 43, as well as far into the superspreading regime, as shown in Ref. 7.

Afterwards, simulations of the surfactant-laden droplet were equilibrated for 1 ns in the *NVT* ensemble at 300 K. To obtain fully covered droplets, we generated starting structures with different numbers of surfactant molecules at the interfaces. After equilibration, the shape of the droplets was examined. Droplets with overcrowded surfaces could easily be identified by the strong deviation from a circular droplet shape at the end of the equilibration period. Droplets with maximum surfactant concentration at the surface with only small deformations of the droplet were used in the spreading simulations.

Equilibration simulations were performed with Nosé-Hoover thermostats and barostats.[44–46] The damping factors were set to $\tau_T = 100$ fs for the thermostat and $\tau_p = 1000$ fs for the barostat. Integration was performed with a four-stage, multiple-timestep rRESPA algorithm,[47] with a factor of two difference in the frequency of force evaluations between adjacent levels. Bonded interactions were evaluated in the innermost stage with a timestep of 0.5 fs. On the second level, we evaluated pair interactions within 6.0 Å, with interactions smoothly shifted to zero beginning at 4.5 Å. On the third level, pair interactions up to a distance of 10.0 Å were computed, with the potential shifted to zero starting at 8.0 Å. Long-ranged interactions were computed on the outermost level.

The initial configurations for the spreading simulations were assembled from the pre-equilibrated polymer slabs and droplets. The starting configurations for the spreading simulations are depicted in Figure 2 for the different surfactants. The droplet radius for the T11 simulation was chosen to be larger because the surfactant was larger. We also note that although the droplet diameter for this surfactant was larger, fewer molecules can exist at the interface for this surfactant, because of the overlap of the hydrophilic tails resulting from the strong curvature of the nanoscale droplet. Further details on the simulation setup and the computational effort of the simulations is given in the Supporting Information.

(a) PP, T3 (b) PP, T6

(c) PP, T11 (d) PP, CE
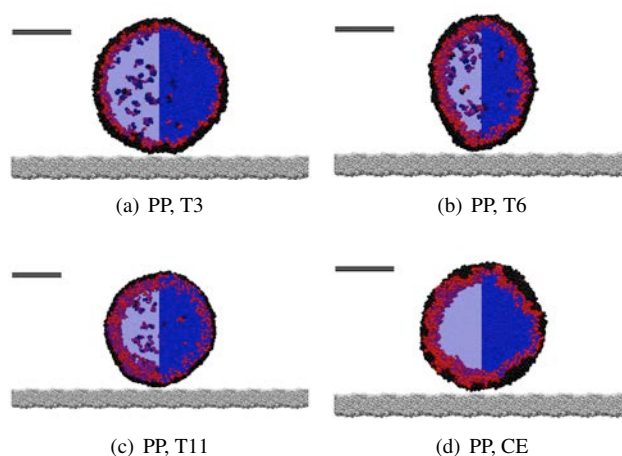
Fig. 2 Snapshots of the starting configurations in simulations with (a) T3, (b) T6, (c) T11, and (d) CE on a PP substrate. Gray: substrate; blue: water; red and black: hydrophilic and hydrophobic part of the surfactant. The left half of the water of each droplet is transparent. The black bar in each figure has a length of 10 nm. This figure and all other visualizations of the snapshots in this article were created with VMD.[48]

The choice of the thermostat can influence the simulation results in non-equilibrium simulations such as the spreading simulations reported here. Specifically, Heine et al.[49] showed that spreading velocities can be affected by the thermostat, which is why we performed our simulations with two different thermostatting strategies. In the first approach, labeled LN below, the lower 5 Å of the substrate were held rigid, while the region from 5 Å to 10 Å was coupled to a Langevin thermostat[50] to serve as an energy sink. The rest of the droplet was integrated using Newtonian dynamics. In a second approach, labeled NH below, the lower 5 Å of the substrate were also held rigid. The rest of the droplet was very weakly coupled to a Nosé-Hoover thermostat with damping factor $\tau_T = 10$ ps. Because of the relatively large system size with $\approx 3 \times 10^5$ par-

ticles and the large coupling constant τ_T, the thermostat has a negligible effect on the dynamics. [45]

We used the PPPM algorithm to compute both long-range electrostatics [51] and dispersion [52,53] interactions in all simulations. Settings for the PPPM were as suggested in Ref. 53. In spreading simulations, we used a two-stage rRESPA, with a factor of two between the inner and outer timesteps. The inner timestep, on which bonded and pair interactions up to 7.0 Å were computed, was 1 fs. Nonbonded interactions on the inner level were shifted to zero between 6.5 Å and 7.0 Å. Long-ranged interactions were computed on the outer level. All simulations were performed with the LAMMPS MD package with in-house modifications described in Ref. 33. Videos of the simulation setup and an example of the spreading process are given in the Electronic Supplementary Information.

2.2 Analysis

Here, we describe the methods used in our analysis. In addition to properties reported here, we computed velocity fields and local temperatures. Results obtained for these quantities are given in the Supporting Information.

2.2.1 Droplet Geometry and Spreading Exponents.
The base width of a droplet is the width of the solid–liquid contact area. Although the lower area of the droplet is not a circle in our simulations, we will in the following use the commonly used term "base radius" r for half of the base width. For the droplet simulations reported here, several challenges need to be overcome to compute the base radius. First, as the polymer substrate is flexible and amorphous, its surface is not as planar as those of crystalline substrates. Hence, a definition of the exact position z_{base} of the surface is not obvious. Second, if there are precursors or feet close to the three-phase contact line, the shape of droplets can deviate from their macroscopic spherical or cylindrical cap shapes. [10] In an MD simulation, which can resolve such deviations in the droplet shape, the base radius of the droplet right at the substrate surface is thus not necessarily comparable to the value reported in experiments.

The base radius r is computed in two steps. In the first step, we define the position of the solid–liquid interface z_{base}. A histogram of the density of the water and surfactant molecules is computed with 1 Å-wide bins in the x and z-dimensions using a procedure similar to that of Ref. 54. The densities are averaged over 10 ps, a time scale long enough to obtain data that is not too noisy, but also short enough to avoid distortion of the data because of changes in droplet shape that occur on much larger time scales. From the density histogram, the droplet domain is determined. Because the vapor phase is almost empty and the interface has a steep density gradient, the domain can be simply defined according to the density: any bins whose density is larger than 10 percent of the maximum

density is considered "inside" the droplet. Bins considered inside the droplet but next to a vapor element are considered boundary elements. Next, we compute a histogram of the z position of the boundary elements. For small values of z, the histogram has a peak which results from the flat surface close to the substrate. The position of the peak is used as the base position z_{base} of the droplet. The procedure of defining z_{base} is illustrated in Figure 3.

In the second step, we use a method similar to that suggested by Halverson et al. [30] to compute the base radius r. As base radius, we use half the width of a rectangular cuboid that contains a fraction p of all atoms within a distance h from the base position z_{base} of the droplet. We tried different values for h and p and found that results, especially for the spreading exponent, are insensitive to these parameters. In the following, we report results for $h = 10$ Å and $p = 0.99$.

Different spreading regimes were determined from log-log plots of the base radius over time. The spreading exponents were determined from fitting straight lines to the linear regimes of the log-log data.

The height h_d of the droplet is defined as the difference between the highest boundary element of the droplet and the base position of the droplet. If we assume that the droplet is a cylindrical cap, the contact angle θ can be computed from

$$h_d = \frac{r(1 - \cos\theta)}{\sin\theta}. \tag{2}$$

To examine the macroscopic droplet shape we fit the droplet boundary to a circle. In the fit, we include only points of the boundary farther than 50 Å from the base position z_{base}. This still leaves a sufficiently large fraction of the droplet to be included in the fit while eliminating the influence of the base region of the droplet. We note that strong deviations of the spherical droplet shape were observed in previous super-spreading studies. [24,55] This deviation, however, occurs in the superspreading regime and is possibly related to inertia and effects caused by surface tension gradients, [24] neither of which can be captured in nanoscopic simulations. A circular fit is thus applicable, as is also visible from Figure 3 and will be briefly validated later in Section 3.2.

2.2.2 Interfacial Surfactant Concentration.
Surfactants are considered adsorbed at the interfaces if their central atom (defined in Figure 1) is within 15 Å of the droplet boundary. Among these surfactants, those whose central atom is within 15 Å of the substrate are classified as adsorbed to the solid–liquid interface, whereas the others are classified as adsorbed to the liquid–vapor interface. All other surfactants are considered as not adsorbed but in the interior of the droplet. The value of 15 Å was chosen because it gives a reasonable separation of the different regions, as shown in Figure 3. The total surface area of the droplet is approximated by the num-
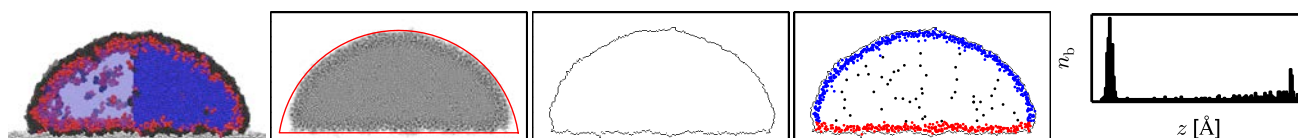
Fig. 3 Analysis steps. Left: Simulation snapshot. Second from left: Density, with a circular fit defined from the boundary elements, and a horizontal line at z_{base}. Middle: Boundary elements. Second from right: position of the center surfactant atoms given in Figure 1. The atoms are labeled according to whether they are classified as at the liquid surface (blue), solid–liquid interface (red), or in the bulk (black). Right: Histogram of the z position of the boundary elements. z_{base} is the z position of the highest peak.

Fig. 4 Steps to classify the local shape of the droplet. Left: input image for the Mumford-Shah segmentation; middle: separated condensed and vapor domains; right: droplet surface, the color code denotes the value of the surface classifier $C(x)$. The surface classifier identifies sharp transitions at both leading edges of the droplet.

ber of border elements. The size of the bottom area is approximated by the number of border elements of the droplet less than 15 Å above the base position; the rest of the droplet surface is classified as part of the liquid–vapor interface. The surfactant concentration at the solid–liquid interface Γ_{sl} is the number of surfactants at the interface divided by the size of the interface.

2.2.3 Moment-Based Surface Analysis of the Droplet Shape.

Differences in droplet shape at the contact line were quantified using a two-step approach based on image analysis. First, we use the binary Mumford-Shah segmentation model[56] to define the location of the droplet interface. Next, we apply the moment-based analysis algorithm for implicit surfaces of Berkels et al.[57] to locally classify the surface of the droplets. The entire process is illustrated in Figure 4.

Here, we use the binary Mumford-Shah segmentation functional

$$E(\rho_c, \rho_v, \Omega_c) = \int_{\Omega_c} (\rho - \rho_c)^2 dA + \int_{\Omega \setminus \Omega_c} (\rho - \rho_v)^2 dA + \eta \text{Per}(\Omega_c), \tag{3}$$

where ρ is the histogram of the local densities of the droplet (cf. Section 2.2.1), ρ_c and ρ_v are the constant densities of the condensed and vapor phase, Ω is the computational domain, Ω_c and $\Omega \setminus \Omega_c$ are the domains of the condensed and vapor phase, and $\text{Per}(\Omega_c)$ is the perimeter of Ω_c in Ω, which is essentially the length of the interface between the condensed and vapor phase. The interface of the system is defined by minimizing Eq. 3 with respect to ρ_c, ρ_v, and Ω_c. The last term

in the functional is a penalty term; η is a parameter that controls the weight of this term and can be adjusted to control the smoothness of the generated segmentation. Large values of η lead to smaller interfaces by smoothening edges. We used $\eta = 0.005 \, \text{g Å cm}^{-3}$ because it provided smooth droplet shapes while preserving the shape of the droplet well. For the minimization with respect to the set Ω_c, the unconstrained convex reformulation proposed in Ref. 58 is used. The resulting convex minimization problem is solved using a first-order primal-dual algorithm[59]. For fixed ρ_c and ρ_l, we can find a global minimizer of the non-convex binary segmentation problem. The Mumford-Shah segmentation was performed with the quocmesh library.[60]

The contour of the computed condensed phase is classified using a moment-based surface analysis. The zero moment shift of the boundary of the object Ω_c is defined as $M_\varepsilon^0[\Omega_c](x)$

$$M_\varepsilon^0[\Omega_c](x) = \frac{1}{\pi \varepsilon^2} \int_{B_\varepsilon(x)} d_{\Omega_c}(y)(y - x) dy, \tag{4}$$

where x is a point on the boundary of Ω_c, the integral is performed over a disk $B_\varepsilon(x)$ centered at position x with radius ε, and $d_{\Omega_c}(y)$ is the signed distance function of Ω_c. The distance function gives the Euclidean distance of any point in the image to the boundary of the object. The signed distance function is equal to the distance function with the difference that it is defined as positive outside the object and as negative inside the object. The surface classifier $C(x)$ is defined from the surface moment as

$$C(x) = g_\beta(\|M_\varepsilon^0[\Omega_c](x)\|/\varepsilon^2), \tag{5}$$

where

$$g_\beta(t) = \frac{1}{1 + \beta t^2}. \tag{6}$$

Smaller values of $C(x)$ correspond to flatter regions close to a position x on the surface, $C(x)$ can thus be used to locally characterized the surface. We note that g_β monotonically maps $\|M_\varepsilon^0[\Omega_c](x)\|/\varepsilon^2$ into the interval $(0,1)$. The use of this function is motivated in Ref. 57. The function or the included parameter β only scale the results and do not qualitatively change them. The only parameters that qualitatively influences the results is the radius of the disk ε, which defines the
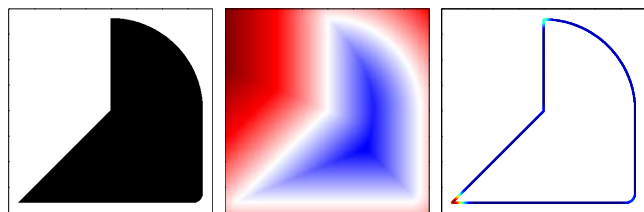
Fig. 5 Example of the moment-based surface analysis. Left: Example shape for the analysis; middle: signed distance function in the image domain; right: surface of the shape color coded with value of the surface classifier $C(x)$.

order of magnitude on which the surface should be characterized. The value of ε should therefore be chosen similar to the magnitude of the feature that is to be identified. Results below are therefore reported for $\varepsilon = 20\,\text{Å}$, being approximately the size of local radius at the contact line for the PP, T6 simulation. The value of β in g_β is set to 20.

An example of the moment-based surface analysis and important features of the resulting classifier are briefly visualized in Figure 5. Based on the surface classifier, it is possible to discriminate edges and smooth regions. The regions at the lower left and at the upper center are identified as edges. The smooth region at the lower right can be discriminated from the sharp edges. Another important feature of the classifier is that the difference between small angles, such as in the lower left of the image, and wider angles, such as in the upper center, is recognized. The latter effect has important implications for the application of this method to our results, because the classifier is influenced by the contact angle θ of the droplet.

3 Results

3.1 Spreading Regimes and Exponents

We first comment on the absolute value of the base radius over time. At first glance, the upper part of Figure 6, which shows the base radius r of the droplet as a function of time in a log-log representation of the LN simulations, suggests that the droplet covered with alkyl ethoxylate surfactants spreads more rapidly than the superspreading droplet, because the base radius r is larger at any given time. However, the base radius depends on several quantities, such as the total volume of the droplet (Eq. 1 is just a proportionality condition). Moreover, deviations from a perfect circular droplet shape, as seen in Figure 2, can distort the spreading velocities in the inertial regime. Consequently, the base radius of the alkyl ethoxylate-laden droplet is larger than the base radius of the trisiloxane-laden droplet. In contrast to the base radius, the spreading exponent α in the viscous regime is not influenced by these effects but arises from the underlying physics. It is thus the

quantity that best describes the spreading. That α is larger for the simulation with the superspreader shows that the droplet spreads faster than in the non-superspreading simulations.
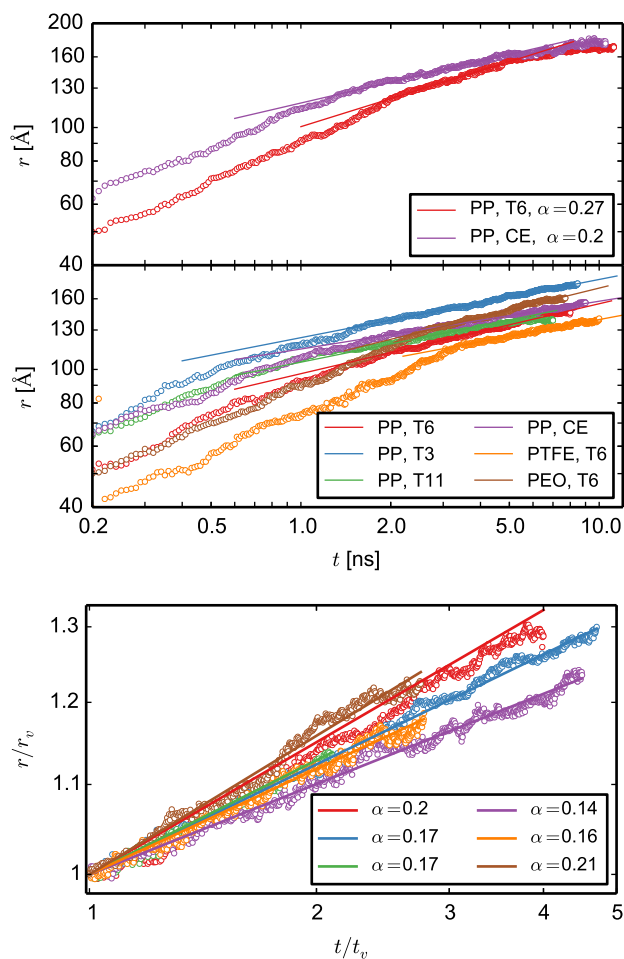
Fig. 6 Base radii r as a function of the simulation time t in log-log representation and lines to determine the spreading exponent. Top: LN simulations; middle: NH simulations; bottom: results from the viscous regime from the NH simulations normalized such that differences between the lines are highlighted.

The spreading exponents observed in the different simulations and the time intervals of the different spreading regimes are given in Table 1. Similar to experimental observations, the spreading passes through several regimes. The first regime is characterized by large spreading exponents. The spreading exponent in this regime is similar to the inertial regime in macroscopic experiments,[12] although the transition time between the first and the second regime occurs for larger characteristic inertial times $\tau_c \propto \left(\rho R^3/\gamma\right)^{1/2}$, where ρ is the liquid density, R is the initial radius of the droplet, and γ is the surface tension of the liquid. For macroscopic droplets, the tran-

thermostat	substrate	surfactant	inertial regime		viscous regime		superspreading[a]
			t [ns]	α	t [ns]	α	
LN	PP	T6	0.2 to 2.4	0.39	2.4 to 5.2	0.27	yes[39]
	PP	CE	0.2 to 2.0	0.34	2.0 to 5.2	0.20	no[30]
NH	PP	T6	0.2 to 2.0	0.34	2.0 to 8.0[b]	0.20	yes[39]
	PP	T3	0.2 to 1.8	0.29	1.8 to 8.47[b]	0.17	no[6]
	PP	T11	0.2 to 2.0	0.25	2.0 to 4.2	0.17	no[6]
	PP	CE	0.2 to 2.0	0.28	2.0 to 9.0[b]	0.14	no[30]
	PTFE	T6	0.3 to 3.6	0.37	3.6 to 10.0[b]	0.16	no[39]
	PEO	T6	0.2 to 2.8	0.37	2.8 to 7.7[b]	0.21	no[3,40]

Table 1 Spreading exponents and duration of different spreading regimes. [a] "Yes" indicates superspreading is experimentally observed at these conditions. References to the corresponding experimental literature are indicated. [b] End of reported viscous regime corresponds to end of the simulation.

sition time is $\tau \approx \tau_c$,[12] whereas in our simulations the transition time is $\tau \approx 100\tau_c$, with $\tau_c \approx 10$ ps. This large difference is potentially caused by the small length scales in our simulations compared to experiments, or could result from using cylindrical droplets instead of the spherical droplets used in experiments.

The second regime is the viscous regime, characterized by a lower spreading exponent. For this second regime, linear fits used to determine the spreading exponent are shown in Figure 6. The measured data are approximately on a straight line in this regime. At later times in the LN simulations, spreading slows down and the curves level off. In this third regime the surfactant concentration at the interfaces decreases. Moreover, because of the thermostatting strategy, the temperature strongly increases in LN simulations. As a result, the driving force for spreading weakens.

The third regime is a result of the simulations being performed at the nanoscale; a connection to the macroscale is difficult and further investigation of this regime is unlikely to enhance understanding of superspreading. For the inertial regime, no relevant differences were found between superspreading and non-superspreading surfactants.[18] For the second, viscous regime, however, significant differences between superspreading and non-superspreading solutions were observed.[18] The behavior of droplets and especially the spreading exponents in this regime are thus of interest here. Because of the nanoscale domain and cylindrical geometry of our simulations, it is clear that not all experimental features can be reproduced. The spreading exponent in the viscous regime, however, should mainly depend on microscopic features. We therefore expect that we should at least be able to approximately reproduce experimental findings.

For the viscous regime, we find that the spreading exponent for the superspreading surfactant is greater than the spreading exponent for the non-superspreading solution in LN simulations. However, comparing the spreading exponents observed by Wang et al.[18] with ours, and considering the different geometries (spherical in experiment and cylindrical in simulation), the spreading exponents in the LN simulations appear to be too large: Wang et al. observed spreading exponents $\alpha \approx 1/7$ for superspreading and $\alpha \approx 1/10$ for non-superspreading solutions, which corresponds to the MKT and the HDM. We therefore would expect to find exponents of $\alpha \approx 1/5$ and $\alpha \approx 1/7$. However, the observed spreading exponents are larger (cf. Table 1).

When examining the temperature of the LN simulations, we noticed that during the simulation the temperature increased by more than 100 K, indicating that the heat sink in the Langevin region was insufficient to adsorb the heat generated by dissipation, or the heat could not be transported sufficiently fast to the heat sink. This motivated the NH simulations, in which most of the particles are weakly coupled to a Nosé-Hoover thermostat. In these simulations, the temperature did not increase during the simulation despite the weak coupling. Because we did not expect to recover the superspreading regime in our simulations, NH simulations were stopped when the viscous regime was sufficiently well-developed to determine spreading exponents. The base radius as a function of time is given as log-log data in the middle image of Figure 6; the lower image of Figure 6 shows the data of the viscous regime translated to highlight the differences between the curves. Lines from the fit to determine the spreading exponent are also shown.

For the NH simulations, results are in much better agreement with experimental data.[18] The spreading exponent is smallest for the alkyl ethoxylate surfactant ($\alpha \approx 0.14$); for trisiloxane surfactants with tails too long or too short or where the substrate is too hydrophobic for superspreading, the spreading exponent is $\alpha \approx 0.17$. Considering the inherent noise, the results for these non-superspreading scenarios are in reasonable agreement with the HDM, such as the experiments by Wang et al.[18] with non-superspreading solutions

of trisiloxanes on PP substrates. Given that also their results had some deviations from the perfect $\alpha = 1/10$ behavior, the agreement between our simulations and their experiments is satisfying for these non-superspreading cases. For the super-spreading case, with the T6 surfactant on the PP substrate, the measured spreading exponent is slightly above 0.2, in reasonable agreement with MKT and therefore also in agreement with experimental results.[18] For the PEO substrate, for which no experimental data is available, the spreading exponent is also slightly above 0.2. In summary, the trend that the droplet at superspreading conditions has a higher spreading exponent in the viscous regime is reproduced in the NH simulations, with the only exception being the PEO substrate.

To explore the source of this discrepancy, we note that, as discussed above, differences in spreading exponents suggest that different physical processes underlie the spreading. The reason for the increased spreading exponent for the super-spreading case will be discussed in Section 3.2, whereas the differences in the physical behavior for the PEO simulation compared to the other simulations are addressed here. As described in the introduction, the PEO substrate is hydrophilic and water has an affinity for this substrate. As a result, in our simulations, water diffused to the substrate at the contact line and surfactants desorbed from the substrate, as shown in Figure 7. This desorption of surfactants or even depletion of surfactants close to the contact line was not observed in any other simulation, as can be seen from the surfactant concentration at the substrate Γ_{sl} decreasing much less rapidly for all other substrates compared to PEO. We therefore suggest that the increased spreading exponent is a result of water diffusing to the contact line region. It is unclear, however, how exactly this process increases the spreading exponent. Because the depletion of surfactants at the contact line caused by water diffusing to the droplet edge occurs on nanoscopic time and length scales, it is unclear whether this increased spreading exponent can be reproduced in experiments.

3.2   Droplet Shape

As outlined in the introduction, a molecular understanding of phenomena at the contact line is of great interest to better understand superspreading. Snapshots of the droplets of the different NH simulations with the circular fit to the droplet shape are depicted in Figure 8. MD simulations with simple model molecules by Shen at al.[29] suggested that bilayers might form in spreading droplets with trisiloxane surfactants. In our larger, more realistic simulations, however, it is immediately apparent that neither a bilayer nor a precursor forms. Likewise, feet are not visible, which argues against superspreading hypotheses based on precursor formation. These results also show that the approximation of the droplet shapes with cylindrical caps is reasonable.
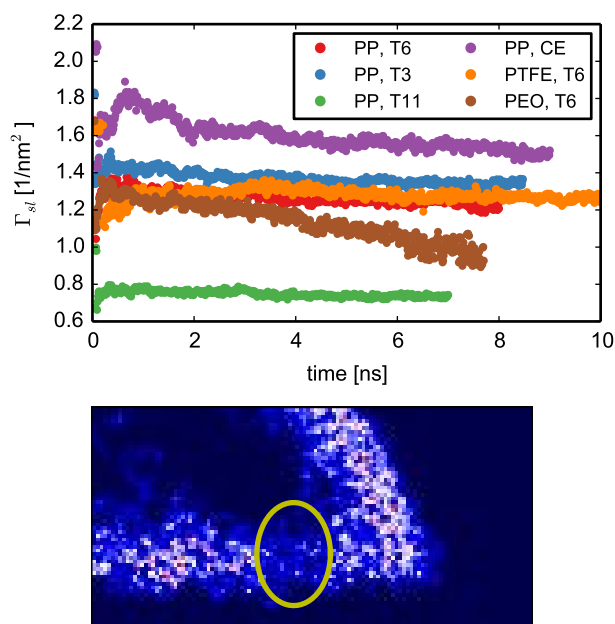
Fig. 7 Top: Surfactant density Γ_{sl} at the solid–liquid interface (computed as described in Section 2.2.2) for the different NH simulations. For the simulation on PEO, the surfactant density drops more rapidly because of unfavorable surfactant adsorption on the substrates compared to water adsorption and the resulting surfactant desorption from the substrate. Bottom: Surfactant density close to the three phase contact line for the PEO simulation. The region at the substrate close to the contact line (enclosed by the yellow ellipse) shows surfactant depletion, which is obvious from the absence of red and very limited presence of white spots.

We continue with the results obtained with the moment-based surface analysis. The differences between some of the non-superspreading cases compared to the superspreading case is immediately visible from Figure 9, which shows the surface of the final snapshot of the viscous regime of each simulation color coded with the surface classifier. The droplet at superspreading conditions (PP, T6) has a smooth transition at both droplet edges, as can be seen from the shape and also from the color code for the surface classifier $C(x)$. For the simulations at non-superspreading conditions with short surfactants (PP, T3), the alkyl ethoxylate surfactant (PP, CE), and the too-hydrophilic surface (PEO, T6), the leading edges of the droplet are much sharper. For the remaining cases (PP, T11 and PTFE, T6), the difference compared to the superspreading case (PP, T6) is not readily visible from Figure 9. It will be shown below that the difference for the PP, T11 case cannot be well detected from Figure 9 because of the difference in sampled contact angles.

To demonstrate the differences between the observed shapes more quantitatively, we analyze how the shape evolves
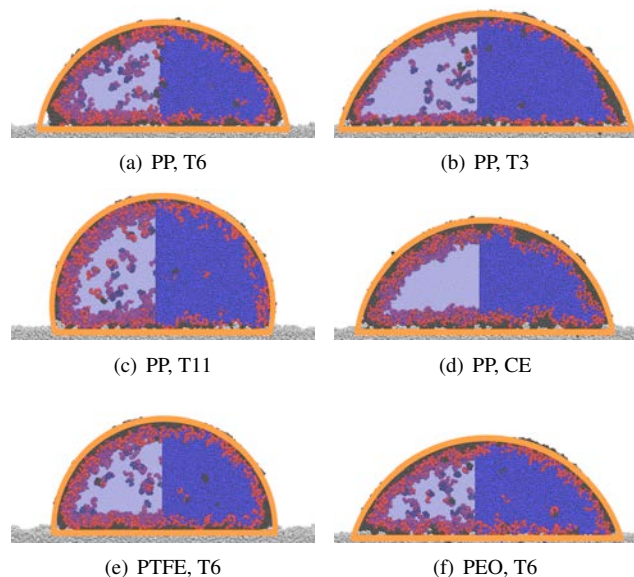
Fig. 8 Simulation snapshots from the NH simulations in the viscous regime. The orange lines are the circular fit and a horizontal line at the base position z_{base}. No bilayer, precursor, or foot is formed in any of the simulations.

Fig. 9 Droplet shapes from the NH simulations in the viscous regime color coded with the classifier $C(x)$.

over the simulation time. For each simulation snapshot in the viscous spreading regime, we determine the maximum value of the surface classifier C_{max} at the left and right corners. These values are plotted in Figure 10 versus the macroscopic contact angle θ determined from Eq. 2. In each subfigure, we include data for the superspreading case and one non-superspreading case to permit direct comparison. The bright and dark shades of the colors corresponds to the values obtained at the left and right edge, respectively. C_{max} is plotted over θ because θ has an impact on C_{max}, as briefly described in Section 2.2.3. Note that the time is implicitly included in Figure 10, because with increasing simulation time, θ decreases; points in the diagram that are further to the left are therefore on average from later simulation times than those to the right. Because of the noise in the results, the values in Figure 10 are cloud points. In the chosen representation, data points obtained from droplets with smoother edges lie on average below those with sharper edges.

The differences between the superspreading droplet and non-superspreading cases with a too-short (PP, T3) or alkyl ethoxylate (PP, CE) surfactant, and the too-hydrophilic substrate (PEO, T6) can be detected well from Figure 10, which shows a difference in the droplet shape at superspreading conditions and the three non-superspreading cases just mentioned. We note that the differences between the computed values for the classifier are numerically small (e.g., $C_{\text{max}} \approx 0.53$ for PP, T6 and $C_{\text{max}} \approx 0.59$ for PP, CE for small θ), however, these small differences in numbers correspond to the strong differences visible in Figure 9.

Differences can also be seen for the too-large surfactant (PP, T11). Because the contact angles for this case were sampled mainly at larger values compared to all other simulations, the distinction is less obvious. Considering, however, that the surface classifier tends to grow with decreasing contact angle, the observed results suggest that a difference also exists here. The only case where the results obtained with the superspreading case and the non-superspreading case cannot be distinguished is the too-hydrophobic substrate (PTFE, T6). In agreement with Figure 9, one edge of this droplet seems to be sharper than what is observed at superspreading conditions, whereas the other is smoother. The unequal shape of the left and right contact-line region for this simulation might be a result of simulation noise or contact line pinning caused by inhomogeneity of the substrate.

To summarize the results, using the surfactant classifier we can demonstrate that the contact line transition for the superspreading droplet is smooth. For non-superspreading conditions, except the case where the substrate is too hydrophobic, the transition from the droplet to the substrate is sharper. At conditions where the substrate is too hydrophobic, a distinction from the superspreading case was not possible.
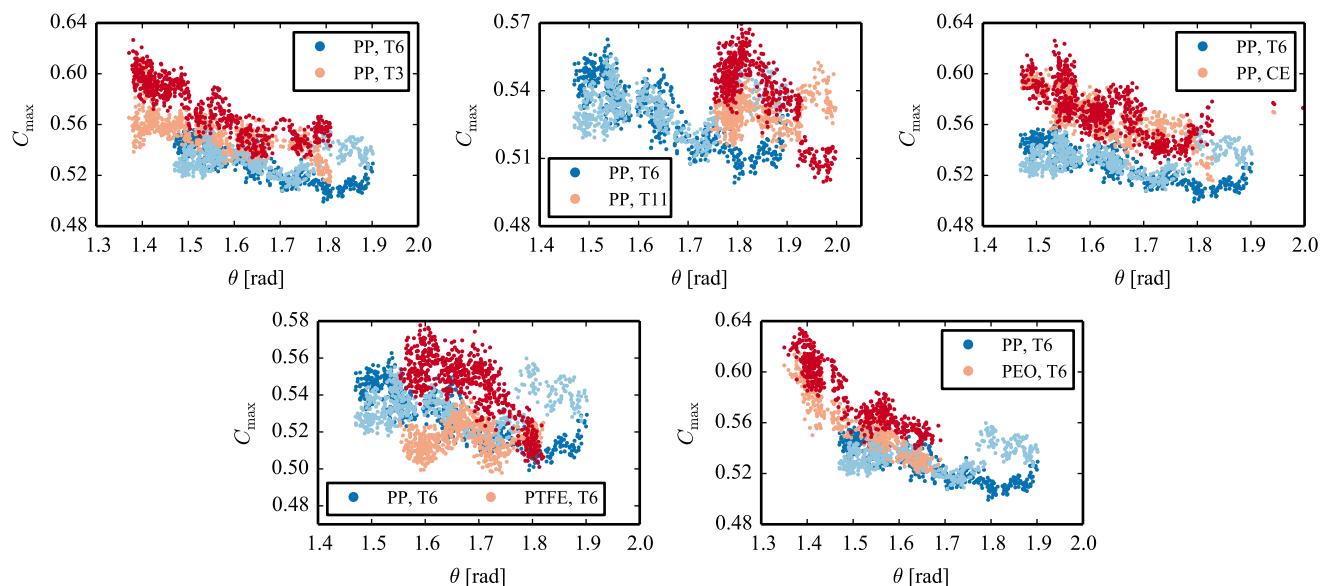
Fig. 10 Maximum droplet classifier C_{max} of the left and right edge of the droplet over the contact angle during the viscous spreading regime. The bright and dark shades of the symbols are the results for the left and right edge of the droplet.

4 Discussion

Two remarkable features of the simulation at superspreading conditions are that the contact line lies behind the circular fit and that the transition from the liquid–vapor to the solid–liquid interface is smooth. This unusual mechanism, to our knowledge, has previously been observed only in the model LJ surfactant study of McNamara et al.[27] This transition removes the sharp edge at the contact line and can thus overcome the Huh–Scriven paradox.[13] It may therefore possibly explain why the spreading exponent in the viscous regime is greater for this case in experiment and our simulation.

As mentioned above, Karapetsas et al.[24] showed that superspreading can occur if direct surfactant adsorption through the contact line is possible and surfactants are soluble. While the latter condition is known to be fulfilled for trisiloxane surfactants, the direct adsorption mechanism remained obscure. The smooth transition from the liquid–vapor to the solid–liquid interface explains how direct adsorption through the contact line can work, as sketched in Figure 11. This smooth contact-line transition can therefore potentially be the molecular mechanism of superspreading. This figure also contains snapshots demonstrating that the suggested mechanism has indeed been observed in simulations. In the following, we will discuss why this smooth transition was observed in simulation at superspreading conditions and relate this to the complex dependencies of the superspreading mechanism on the surface energy of the substrate and the surfactant chain length.

The smooth transition between the interfaces requires a strong bending of the droplet surface close to the contact line. This bending is associated with an energy penalty and will thus only occur if the penalty is compensated for by an energetically favorable feature. We hypothesize that this feature is the existence of an unbroken surfactant aggregate at the interfaces; the existence of these aggregates for superspreading trisiloxane surfactants was shown by Ritacco et al.[61] on planar interfaces. That the smooth transition only occurs for the superspreading scenario at intermediate values of the chain length of the surfactant is a logical consequence of this hypothesis. Although we cannot measure the existence of these aggregates from our simulation output, the existence of stable aggregates that connects the vapor–liquid and the solid–liquid interface is the only mechanism that we can think of that provides a reasonable explanation for the smoothing of the contact line.

The chain length of the surfactants affects the energy penalty associated with the bending of the interface and the stability of the aggregates. For too-long surfactants, the hydrophilic parts overlap and repel each other when the interface is bent, which is why this state is energetically unfavorable and surfactant aggregates will break up. For too-short surfactants, aggregates at the interface are not formed, as shown experimentally in Ref. 61. Thus, intermediate values for the chain length are best to facilitate the smooth transition at the contact line.

For surfaces that are too hydrophilic, like PEO, the adsorption of the surfactant is unfavorable because the surface prefers contact with water. This can be seen from the surfac-

(c) superspreading (d) non-superspreading
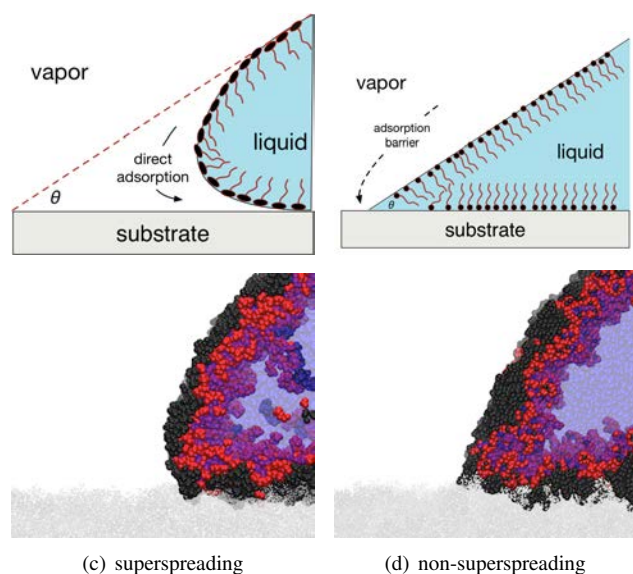
Fig. 11 Top: A sketch of the proposed mechanism for superspreading compared to usual surfactant enhanced wetting. Gray: solid; blue: water; black and red: hydrophilic and hydrophobic parts of the surfactants. The angle θ is the macroscopic contact angle of the droplet. For the superspreading case, the contact line is bent inwards, allowing for direct surfactant adsorption on the substrate. The hydrophilic tails are long enough to form aggregates, but not so long as to overlap and repel each other in the bended region. The compact head group and the relative size of the head and tail groups enhance the stability of these aggregates. The preferable adsorption energies and that aggregates are not torn apart compensate the energy penalty for bending. For the conventional surfactant enhanced spreading, the surfactant aggregates are torn apart: surfactants must reorient at the contact line, thus imposing an adsorption barrier. Bottom: Simulation snapshots from PP, T6 and the PP, CE showing that simulation results indeed resemble the proposed mechanism.

tant density at the solid–liquid interface in Figure 7, which shows that the surfactant concentration on the PEO substrate drops more rapidly than on the other substrates, indicating that surfactants desorb from the interface or are repelled by water close to the contact line, which will break the surfactant aggregates.

For the simulations with a substrate that is too hydrophobic, our simulations suggest that the transition from the liquid-vapor interface is smooth, and thus the fast adsorption through the contact line is in principle possible. That the path can occur, however, does not necessarily mean the the surfactants will take this path to adsorb rapidly onto the substrate: Surfaces with low surface energies, such as PTFE, have weak interactions not only with water, but also with the surfactants. Adsorption on these surfaces is thus not very favorable. A possible explanation could also be that our model is not suffi-

ciently accurate for that substrate.

The contact-line mechanism at superspreading conditions observed in this study does not explain why spreading rates are greatest for intermediate surfactant concentrations, or more precisely, why spreading rates are maximal right before a phase transition from vesicles to lamellar phases inside the droplet. This is unrelated to the mechanism at the contact line, but is related to how fast surfactants can be transported from the bulk to the interfaces. In the vesicular solution, surfactant transport accelerates with increasing surfactant concentration; however, when surfactants are in lamellar phases, the surfactants must pass through a phase transition before they can adsorb to the interfaces. Thus, surfactant transport to the interfaces is slower above the phase transition.

5 Conclusions

We report large-scale MD simulations of surfactant-enhanced spreading of aqueous solutions of different trisiloxane and alkyl ethoxylate surfactants on PP, PEO, and PTFE substrates with force fields specifically optimized to study spreading problems.[33] We cover simulation setups in which superspreading occurs in experiment, as well as simulations at various conditions that are unfavorable for superspreading, namely that the surfactant is too short or too long, the substrate is too hydrophilic or too hydrophobic, or because the surfactant does not belong to the general class of superspreading agents.

To have simulation conditions as close to macroscopic experiments as possible, we examine two different thermostatting strategies. In both approaches, the lower part of the substrate is held rigid. In one approach, most of the dynamics are described by Newton's equations of motion and only parts of the substrate are controlled with a Langevin thermostat, whereas in the second approach the entire simulation—except the rigid part—is weakly coupled to a Nosé-Hoover thermostat. In simulations with Langevin and Newtonian dynamics, heat transfer to the heat sink in the Langevin region is insufficient to maintain a constant droplet temperature. As a result, the observed spreading rates are in disagreement with experiments. With the second approach, however, temperature is conserved and agreement with experimental observations for the spreading exponents is achieved. The main difference between our simulations and experiments is that the transition between inertial and viscous spreading was shifted to larger multiples of the characteristic inertial time τ_c.

Under superspreading conditions, we observed a smooth transition at the contact line. This smooth transition removes the sharp edge typically encountered in spreading droplets and thus can overcome the Huh–Scriven paradox. This offers an explanation for the greater spreading exponent observed in the viscous regime at superspreading conditions. An increased

spreading exponent was also observed for aqueous solutions of trisiloxane droplets on a PEO substrate too hydrophilic for superspreading. The increased spreading exponent for this simulation might be a result of water adsorbing to the substrate close to the contact line.

While our simulations are apparently too small to capture Marangoni stresses and therefore cannot directly observe superspreading, our simulation results provide insight about mechanisms at the contact line. The absence of bilayers, precursors, or feet casts doubt on the majority of proposed superspreading hypotheses. In contrast, at superspreading conditions the droplet is bent inwards at the contact line and the transition of the liquid–vapor to the solid–liquid interface is smooth. This smooth transition allows direct surfactant adsorption through the contact line and in this way provides an explanation for the superspreading mechanism.[24] Based on this mechanism, we provide plausible explanations for the complex dependency of superspreading on the substrate hydrophobicity, the surfactant chain length, and the surfactant concentration.

The simulation results reported here show a molecular mechanism at the contact line that potentially enables the fast wetting kinetics of superspreading and illustrates why the effect is not observed under conditions far from the optimum. However, the results reported here do not explain the difference between conditions that both lead to superspreading, such as between two different substrates on which superspreading can occur or different surfactants, such as trisiloxane surfactants with $n = 5$ and $n = 6$. Moreover, because of the larger length and time scales involved in Marangoni flows, the superspreading regime is not captured directly in our simulations. Further modeling to bridge the involved scales will be required to obtain a full understanding of all details of superspreading. Coarse-graining can provide further information on the role of vesicles and phase behavior. To fully capture the effect, however, accurate hybrid continuum and molecular simulation approaches that can cover both the molecular and the continuum scales will be required.[5,62]

Acknowledgment

References

1 O. K. Matar and R. V. Craster, *Soft Matter*, 2009, **5**, 3801.

2 K. P. Ananthapadmanabhan, E. D. Goddard and P. Chandar, *Colloid Surface*, 1990, **44**, 281–297.

3 R. M. Hill, *Curr. Opin. Colloid. Interf. Sci*, 1998, **3**, 247–254.

4 J. Venzmer, *Curr. Opin. Colloid. Interf. Sci*, 2011, **16**, 335–343.

5 P. E. Theodorakis, E. A. Müller, R. V. Craster and O. K. Matar, *Curr. Opin. Colloid. Interf. Sci*, 2014, **19**, 283–289.

6 R. Wagner, Y. Wu, G. Czichocki, H. v. Berlepsch, B. Weiland, F. Rexin and L. Perepelittchenko, *Appl. Organomet. Chem.*, 1999, **13**, 611–620.

7 R. Wagner, Y. Wu, G. Czichocki, H. v. Berlepsch, F. Rexin and L. Perepelittchenko, *Appl. Organomet. Chem.*, 1999, **13**, 201–208.

8 R. Wagner, Y. Wu, H. v. Berlepsch and L. Perepelittchenko, *Appl. Organomet. Chem.*, 2000, **14**, 177–188.

9 G. McHale, C. V. Brown and N. Sampara, *Nat. Commun.*, 2013, **4**, 1605.

10 D. Bonn, J. Eggers, J. Indekeu, J. Meunier and E. Rolley, *Rev. Mod. Phys.*, 2009, **81**, 739–805.

11 R. S. Cowles, E. A. Cowles, A. M. McDermott and D. Ramoutar, *J. Econ. Entomol.*, 2000, **93**, 180–188.

12 L. Chen, E. Bonaccurso and M. E. R. Shanahan, *Langmuir*, 2013, **29**, 1893–8.

13 C. Huh and L. E. Scriven, *J. Colloid Interface Sci.*, 1971, **35**, 85–101.

14 P.-G. De Gennes, *Rev. Mod. Phys.*, 1985, **57**, 827–863.

15 T. D. Blake and J. M. Haynes, *J. Colloid Interface Sci.*, 1969, **30**, 421–423.

16 D. R. Heine, G. S. Grest and E. B. Webb, III, *Phys. Rev. E*, 2004, **70**, 011606.

17 L. H. Tanner, *J. Phys. D: Appl. Phys*, 1979, **12**, 1473.

18 X. Wang, L. Chen, E. Bonaccurso and J. Venzmer, *Langmuir*, 2013, **29**, 14855–14864.

19 J. Radulovic, K. Sefiane and M. E. R. Shanahan, *J. Phys. Chem. C*, 2010, **114**, 13620–13629.

20 A. Nikolov and D. Wasan, *Eur. Phys. J.-Spec. Top.*, 2011, **197**, 325–341.

21 T. Stoebe, Z. Lin, R. M. Hill, M. D. Ward and H. T. Davis, *Langmuir*, 1997, **13**, 7282–7286.

22 A. Kabalnov, *Langmuir*, 2000, **16**, 2595–2603.

23 N. V. Churaev, N. E. Esipova, R. M. Hill, V. D. Sobolev, V. M. Starov and Z. M. Zorin, *Langmuir*, 2001, **17**, 1338–1348.

24 G. Karapetsas, R. V. Craster and O. K. Matar, *J. Fluid Mech.*, 2011, **670**, 5–37.

25 E. Ruckenstein, *Colloid Surface A*, 2012, **412**, 36–37.

26 C. Maldarelli, *J. Fluid Mech.*, 2011, **670**, 1–4.

27 S. McNamara, J. Koplik and J. R. Banavar, *Lect. Notes Comput. Sci.*, 2001, **2073**, 551–559.

28 H.-Y. Kim, Y. Qin and K. A. Fichthorn, *J. Chem. Phys.*, 2006, **125**, 174708.

29 Y. Shen, A. Couzis, J. Koplik, C. Maldarelli and M. S. Tomassone, *Langmuir*, 2005, **21**, 12160–70.

30 J. D. Halverson, C. Maldarelli, A. Couzis and J. Koplik, *Chem. Eng. Sci.*, 2009, **64**, 4657–4667.

31 J. D. Halverson, *PhD thesis*, City University of New York, 2008.

32 P. E. Theodorakis, E. A. Müller, R. V. Craster and O. K. Matar, *Langmuir*, 2015, **31**, 2304–2309.

33 R. E. Isele-Holder and A. E. Ismail, *J. Phys. Chem. B*, 2014, **118**, 9284–9297.

34 J. L. F. Abascal and C. Vega, *J. Chem. Phys.*, 2005, **123**, 234505.

35 R. A. Sorensen, W. B. Liau, L. Kesner and R. H. Boyd, *Macromolecules*, 1988, **21**, 200–208.

36 O. Borodin, G. D. Smith and D. Bedrov, *J. Phys. Chem. B*, 2002, **106**, 9912–9922.

37 O. Borodin and G. D. Smith, *J. Phys. Chem. B*, 2003, **107**, 6801–6812.

38 J. S. Smith, O. Borodin and G. D. Smith, *J. Phys. Chem. B*, 2004, **108**, 20340–20350.

39 N. A. Ivanova, Z. B. Zhantenova and V. M. Starov, *Colloid Surface A*, 2012, **413**, 307–313.

40 C. J. V. Oss, R. J. Good and R. J. Busscher, *J. Dispersion Sci. Technol.*, 1990, **11**, 75–81.

41 *MAPS platform. Scienomics.http://www.scienomics.com*.

42 N. Ivanova, V. Starov, R. Rubio, H. Ritacco, N. Hilal and D. Johnson, *Colloid Surface A*, 2010, **345**, 143–148.

43 T. Svitova, R. M. Hill, Y. Smirnova, A. Stuermer and G. Yakubov, *Langmuir*, 1998, **14**, 5023–5031.

44 M. Parrinello and A. Rahman, *J. Appl. Phys.*, 1981, **52**, 7182–7190.

45 M. E. Tuckerman, J. Alejandre, R. López-Rendón, A. L. Jochim and G. J. Martyna, *J. Phys. A - Math. Gen.*, 2006, **39**, 5629–5651.

46 W. Shinoda, M. Shiga and M. Mikami, *Phys. Rev. B*, 2004, **69**, 134103.

47 G. J. Martyna, D. J. Tobias and M. L. Klein, *J. Chem. Phys.*, 1994, **101**, 4177–4189.

48 W. Humphrey, A. Dalke and K. Schulten, *J. Mol. Graphics*, 1996, **14**, 33–38.

49 D. R. Heine, G. S. Grest and E. B. Webb, III, *Phys. Rev. E*, 2003, **68**, 061603.

50 T. Schneider and E. Stoll, *Phys. Rev. B*, 1978, **17**, 1302–1322.

51 R. Hockney and J. Eastwood, *Computer simulations using particles*, McGraw-Hill Inc., New York, 1988.

52 R. E. Isele-Holder, W. Mitchell and A. E. Ismail, *J. Chem. Phys.*, 2012, **137**, 174107.

53 R. E. Isele-Holder, W. Mitchell, J. R. Hammond, A. Kohlmeyer and A. E. Ismail, *J. Chem. Theory Comput.*, 2013, **9**, 5412–5420.

54 A. E. Ismail, G. S. Grest, D. R. Heine, M. J. Stevens and M. Tsige, *Macromolecules*, 2009, **42**, 3186–3194.

55 S. Rafaï, D. Sarker, V. Bergeron, J. Meunier and D. Bonn, *Langmuir*, 2002, **18**, 10486–10488.

56 D. Mumford and J. Shah, *Commun. Pure Appl. Math.*, 1989, **42**, 577–685.

57 B. Berkels, I. Cabrilo, S. Haller, M. Rumpf and K. Schaller, *Int. J. CARS*, 2014, **9**, 387–400.

58 B. Berkels, Proceedings of the Second International Conference on Scale Space Methods and Variational Methods in Computer Vision (SSVM 2009), 2009, pp. 26–37.

59 A. Chambolle and T. Pock, *J. Math. Imaging Vision*, 2010, **40**, 120–145.

60 AG Rumpf, Institute for Numerical Simulation, University of Bonn, http://numod.ins.uni-bonn.de/software/quocmesh/.

61 H. A. Ritacco, F. Ortega, R. G. Rubio, N. Ivanova and V. M. Starov, *Colloid Surface A*, 2010, **365**, 199–203.

62 M. G. Schmidt, R. A. Sauer and A. E. Ismail, *Modell. Simul. Mater. Sci. Eng.*, 2014, **22**, 045012.

Soft Matter Accepted Manuscript

vapor

direct
adsorption

liquid

θ

substrate